Süleyman Demirel Üniversitesi
Fen Bilimleri Enstitüsü Dergisi
Cilt 30, Sayı 1, 168-183, 2026

Süleyman Demirel University
Journal of Natural and Applied Sciences
Volume 30, Issue 1, 168-183, 2026

DOI: 10.19113/sdufenbed.1805609

Comparative Evaluation of the Load-Carrying Behavior of Fixed-End Steel Beams Using Different Analysis Methods

Mustafa Berker ALICIOĞLU*[1]

[1]MANİSA KENTSEL DÖNÜŞÜM MÜDÜRLÜĞÜ

(Alınış / Received: 17.10.2025, Kabul / Accepted: 27.02.2026, Online Yayınlanma / Published Online: 24.04.2026)

Keywords
Buckling analysis
Steel beam
Plastic analysis
SAP2000

Abstract: This study investigates the behavior of seven steel beams with different cross-sections, each 8 m in length and fixed at both ends, fabricated from S235 steel. The cross-sections were selected in accordance with the requirements specified in Section 9 (Subsections 9.2–9.8) of the Regulation on the Design, Calculation, and Construction of Steel Structures (ÇYTHYDE-2018). The beams were modeled using shell elements, and all analyses were conducted using SAP2000 finite element software. Three analysis methods were employed. First, the theoretical load-carrying capacities of the beams were calculated using the equations provided in ÇYTHYDE-2018. Second, a second-order plastic analysis was performed, in which the midspan load (P) was incrementally increased to determine the beams' plastic capacities. Finally, a buckling analysis was conducted, with the first-mode buckling factor computed to evaluate the beams' flexural, torsional, and lateral-torsional buckling behavior. A comparison between the analytical (code-based) moment capacities and the nonlinear numerical results indicated percentage differences ranging between 1% and 6% for IPE600, HE300AA, Built up I, HE450A, Box, and Pipe sections, whereas the Built up II section exhibited a significant difference of 93.89%. Consequently, it has been revealed that the equations provided in Clause 9.5 of the ÇYTHYDE-2018 specification require revision. The results indicate that the Built up I exhibits pronounced sensitivity to the combined effects of lateral translation and torsion, whereas the Built up II demonstrates a comparatively balanced stability performance among bending, torsional, and lateral–torsional buckling modes. Nevertheless, the initial loss of stability is most likely to occur through the lateral–torsional buckling mode.

Ankastre Mesnetli Çelik Kirişlerin Taşıma Davranışının Farklı Analiz Yöntemleri ile Karşılaştırmalı Değerlendirilmesi

Öz
Burkulma analizi
Çelik kiriş
Plastik analiz
SAP2000

Öz: Bu çalışmada, 8 m uzunluğunda ve uçları ankastre mesnetli olarak tasarlanan, S235 çeliğinden imal edilmiş yedi farklı enkesitli kirişin davranışı incelenmiştir. Enkesitler, Çelik Yapıların Tasarım, Hesap ve Yapımına Dair Esaslar (ÇYTHYDE-2018) yönetmeliğinin 9. bölümünde (9.2–9.8 alt bölümleri) tanımlanan koşulları sağlayacak şekilde seçilmiştir. Kirişler, kabuk eleman olarak modellenmiş ve analizler SAP2000 sonlu elemanlar programı kullanılarak gerçekleştirilmiştir. Çalışmada üç farklı analiz yöntemi uygulanmıştır. İlk olarak, ÇYTHYDE-2018 yönetmeliğinde verilen denklemler kullanılarak kirişlerin teorik taşıma kapasiteleri hesaplanmıştır. İkinci olarak, II. mertebe plastik analiz yöntemiyle kiriş orta noktasına uygulanan tekil yük (P) kademeli olarak artırılmış ve bu yolla kirişlerin plastik kapasiteleri belirlenmiştir. Son olarak, burkulma analizi gerçekleştirilmiş; birinci mod burkulma faktörü hesaplanmış ve bu faktörler ile kirişlerin eğilme, burulma ve yanal burulmalı burkulma davranışları irdelenmiştir. Analitik (yönetmelik esaslı) moment kapasiteleri ile doğrusal olmayan sayısal analiz sonuçlarının karşılaştırılması sonucunda, IPE600, HE300AA, Yapma I, HE450A, Kutu ve Boru kesitlerinde farkın %1 ile %6 arasında değiştiği, buna karşılık narin gövdeli Yapma II kesitinde bu farkın %93,89 seviyesine ulaştığı belirlenmiştir. Sonuç olarak, ÇYTHYDE-2018 yönetmeliğinin 9.5 alt bölümünde yer alan denklemlerin güncellenmesi gerektiği ortaya konmuştur. Yapma I kesitinin özellikle yanal ötelenme ve burulma birleşimi etkilerine karşı duyarlı bir davranış

*Corresponding author: berker.alicioglu@gmail.com

sergilediği ve Yapma II kesitinin genel olarak eğilme, burulma, yanal burulmalı burkulma modları arasında dengeli bir stabilite düzeyine sahip olduğu, ancak ilk stabilite kaybının yanal-burulmalı (lateral-torsional) burkulma modunda gerçekleşmesinin muhtemel olduğu belirlenmiştir.

1. Introduction

Buckling in steel beams is a failure mechanism that limits load-carrying capacity and plays a critical role in ensuring structural stability. At low load levels, beams can safely resist bending and shear effects within the elastic range. However, as the load increases, the fibers in the compression zone tend to deflect out of plane, and beyond a certain critical load level, the linear equilibrium can no longer be maintained, resulting in a sudden loss of stability. This instability typically occurs through the simultaneous interaction of lateral displacement and torsional rotation. Since buckling may occur before the material reaches its yield strength, it becomes a limiting factor in the design of steel beams [1, 2].

Several types of buckling have been identified in the literature. Flexural buckling refers to the out-of-plane deflection of a member subjected to axial compression; torsional buckling occurs when the section fails due to insufficient torsional stiffness; and lateral-torsional buckling (LTB) is defined as the phenomenon in which both lateral displacement and twisting occur simultaneously in beams subjected to bending moments [3]. In particular, LTB becomes a governing factor for the safety of design in slender and thin-walled beams with long spans.

It has been demonstrated in various studies that buckling behavior is not solely governed by cross-sectional geometry, but is also influenced by material properties, boundary conditions, loading configurations, and the arrangement of lateral restraints. For example, [4] experimentally investigated the effects of lateral bracing on the critical buckling load of two-span continuous steel beams and demonstrated that even minimal bracing can significantly enhance buckling resistance. Similarly, [5] examined the LTB behavior of steel beams under impact loading through both experimental and numerical approaches, emphasizing the decisive role of loading rate and cross-sectional dimensions on the buckling modes. In another study, [6] revealed that geometric imperfections and loading eccentricities considerably affect the critical buckling load of tapered thin-walled beams. Moreover, [7] showed that restricting the rotational and torsional degrees of freedom at the support joints has a direct influence on the critical moment. Additionally, researchers such as [8] reported that strengthening with FRP materials is effective in improving the buckling capacity of beams.

Plastic analysis has emerged as an important method for determining the actual load-carrying capacities of steel structural members. Since elastic analysis can only evaluate the behavior up to the yield limit, it often produces conservative results. In contrast, plastic analysis provides a more realistic and economical assessment of structural capacity by considering the condition in which the entire cross-section reaches the yield stress and load redistribution occurs through the formation of plastic hinges [9, 10].

The fundamental concept in plastic analysis is the plastic moment capacity. This capacity is calculated as the product of the plastic section modulus and the yield stress, and it varies depending on the cross-section class. According to [3] and [11], plastic design can only be applied to Class 1 and Class 2 sections that are capable of exhibiting ductile behavior. In semi-compact or slender sections, it is not possible to reach the full plastic capacity due to the occurrence of local buckling.

Various methods have been developed in the literature for plastic analysis. Limit analysis methods determine the upper and lower bounds of the collapse load based on equilibrium and work theorems, while second-order analysis methods reveal the influence of geometrically nonlinear effects on the load-carrying capacity [9]. It has been observed that second-order effects can significantly reduce the collapse load, particularly in long-span steel beams [12]. With the advancement of the finite element method (FEM), plastic analysis has been examined in greater detail; through software such as ABAQUS, ANSYS, and SAP2000, plastic zones within the cross-section, local instabilities, and failure modes have been successfully modeled [11].

In conclusion, the literature indicates that both buckling and plastic behavior play decisive roles in the design of steel beams. Buckling limits the critical moment, particularly in slender and long-span beams, whereas plastic analysis provides more economical and safe design options by accounting for material ductility and cross-section classification. Studies have shown that differences in cross-section class significantly influence the plastic capacity, while the buckling capacity is affected not only by the cross-sectional geometry but also by support conditions, loading configurations, and strengthening strategies.

In this study, the load-carrying capacities of steel beams with different cross-section classes were determined through theoretical, plastic, and buckling analyses, and the results were evaluated in a comparative manner. Accordingly, the existing knowledge in the literature has been expanded, the performance differences of various sections in terms of buckling and plastic capacity have been highlighted, and practical design implications have been provided.

The primary objective of this study is to comparatively evaluate the load-carrying behavior of fixed-end steel beams with different cross-section classes by employing theoretical calculations in accordance with the Regulation on Design, Calculation, and Construction Principles of Steel Structures [11], second-order plastic analysis, and elastic buckling analysis. Although numerous studies in the literature have examined buckling or plastic behavior separately, a comprehensive comparison integrating theoretical design equations with nonlinear finite element analysis results for different cross-section classes remains limited. The significance of this study lies in revealing the interaction between cross-sectional classification, second-order effects, and buckling behavior within a unified analytical framework. The originality of the research stems from the direct comparison between code-based moment capacities and nonlinear numerical results for beams designed under different subsection provisions (9.2–9.8) of the regulation, and from identifying the potential need for revision in Clause 9.5. Therefore, the findings provide both theoretical insight and practical implications for improving steel beam design procedures.

2. Materials and Methods

In this study, steel beams of different cross-section classes were modeled using the finite element software SAP2000. The models were subjected to modal analysis, second-order plastic analysis, and buckling analysis. The load-bearing behavior of the beams was evaluated in a comparative manner by considering the results obtained from theoretical calculations of the steel sections alongside the analysis outcomes.

2.1. Modal analysis

Modal analysis is a fundamental dynamic analysis method used to determine the natural vibration modes of a structure and their corresponding natural frequencies. This analysis is particularly critical for understanding the buckling or dynamic behavior of structural elements. Modal analysis characterizes the displacement patterns of a structure by evaluating and superimposing its free vibration mode shapes. These mode shapes define the configurations in which a structure naturally tends to deform [13].

During the modal analyses, eigenvectors were considered to characterize the dynamic behavior of the structure. Eigenvectors define the mode shapes corresponding to each natural vibration mode and are critical for identifying the regions of the structure that are likely to experience concentrated deformation.

In the study, the analysis was performed considering 12 modes to adequately represent the dynamic response of the beams. This approach encompasses the effects of both low- and high-frequency modes, allowing for a detailed examination of the structure's lateral and torsional deformation characteristics. Consequently, the mode shapes and natural frequencies obtained from the modal analysis were used as fundamental data for evaluating buckling behavior and critical loads.

2.2. Second-order plastic analysis

Second-Order Plastic Analysis is an analytical method that considers both plastic deformations and the geometrically nonlinear behavior of structural frames when evaluating their load-carrying capacity. This type of analysis is particularly important for assessing the stability and overall capacity of frame systems.

In second-order plastic analysis, plastic deformations that exceed the elastic limit of the structure and their effects on the overall structural behavior are examined. During the analysis, plastic hinges may form in the members, and plastic regions may develop within the sections, with the behavior of these regions being thoroughly evaluated. This approach accounts not only for the elastic behavior of the structure but also for geometrically nonlinear effects, providing a more realistic estimation of the load-carrying capacity.

In this context, [14] details second-order plastic-hinge analyses for frame structures under the study titled "Second-Order Refined Plastic-Hinge Analysis for Frame Structures." Similarly, [15], in the study "Simplified Second-Order Inelastic Analysis for Frame Design," presents simplified second-order inelastic analysis methods. These references constitute foundational works that academically support the methodologies and applications of second-order plastic analysis.

In this study, the second-order plastic analysis was performed incrementally by increasing the vertical midspan load until numerical instability occurred. The load–displacement curve was extracted from the bottom midspan node. Yield load (P_y) was defined as the point where deviation from linear elastic response was first observed.

2.3. Shell layered nonlinear

The shell layered nonlinear approach is employed to realistically model structural elements composed of multiple material layers. Within this method, shell elements are defined in multiple layers, with each layer assigned individual thickness, material properties, and nonlinear behavior.

This allows the analysis to incorporate the nonlinear responses of the material, such as plasticity, cracking, or crushing, as well as the complex mechanical characteristics of the layered structure. Implemented in SAP2000, this method enables a more reliable determination of the load–displacement behavior and ultimate load-carrying capacity of reinforced concrete, composite, and steel elements [16].

Similarly, as highlighted by [17], defining shell elements as layered and nonlinear provides a significant improvement in accuracy when modeling material and geometric nonlinearities within the finite element method.

2.4. Buckling analysis

Buckling analysis is a method used to determine the tendency of structural members to become unstable under axial loads or compressive forces and is particularly critical when evaluating the load-carrying capacity of slender bars and beams. Through this analysis, the load levels at which members exhibit buckling behavior beyond the elastic limit, the corresponding critical buckling loads, and the possible buckling modes can be identified.

During the analysis, the geometry of the member, boundary conditions, and material properties are taken into account, and a linear elastic buckling analysis is performed using structural analysis software such as SAP2000. The eigenvalue method is then employed to determine the critical loads and corresponding mode shapes [18]. Buckling analysis provides a fundamental reference for establishing safe load limits and ensuring structural stability, particularly before considering second-order effects and plastic deformations in the design process.

The buckling analysis was conducted as linear eigenvalue buckling. The critical load factor was obtained by multiplying the applied reference load by the calculated eigenvalue. The lowest eigenvalue was taken as the governing stability parameter.

2.5. Theoretical calculations

Theoretical calculations were carried out using the equations provided in Chapter 9 (Clauses 9.2–9.8) of the Regulation on Design, Calculation, and Construction Principles of Steel Structures [11]. The relevant equations for each cross-section type are summarized below.

(i) IPE600 Section

The calculations for the IPE600 section were performed using Equations (1–7):

$$i_{ts}^2 = \frac{\sqrt{I_y C_w}}{W_{ex}} \tag{1}$$

$$L_p = 1{,}76 i_y \sqrt{\frac{E}{F_y}} \tag{2}$$

$$L_r = 1{,}95 i_{ts} \frac{E}{0{,}7F_y} \sqrt{\frac{Jc}{W_{ex}h_0} + \sqrt{\left(\frac{Jc}{W_{ex}h_0}\right)^2 + 6{,}76\left(\frac{0{,}7F_y}{E}\right)^2}} \tag{3}$$

$$C_b = \frac{12{,}5M_{maks}}{2{,}5M_{maks} + 3M_A + 4M_B + 3M_C} \tag{4}$$

$$F_{cr} = \frac{C_b \pi^2 E}{\left(\frac{L_b}{i_{ts}}\right)^2} \sqrt{1 + 0{,}078 \frac{Jc}{W_{ex}h_0}\left(\frac{L_b}{i_{ts}}\right)^2} \tag{5}$$

$$M_n = F_{cr} W_{ex} \leq M_p \tag{6}$$

$$M_n = F_{cr} W_{ex} \leq M_p \tag{7}$$

(ii) HE300AA Section

The calculations for the HE300AA section were performed using Equations (7, 8):

$$M_n = M_p - \left(M_p - 0{,}7F_y W_{ex}\right)\left(\frac{\lambda_f - \lambda_{pf}}{\lambda_{rf} - \lambda_{pf}}\right) \tag{8}$$

(iii) Built up I Section

The calculations for the Built up I section were performed using Equations (4, 7, 9–14):

$$i_t = \frac{b_{fc}}{\sqrt{12\left(1 + \frac{1}{6}\frac{h_c t_w}{b_{fc} t_{fc}}\right)}} \tag{9}$$

$$L_p = 1{,}1 i_t \sqrt{\frac{E}{F_y}} \tag{10}$$

$$\frac{W_{ext}}{W_{exc}} \geq 0{,}7 \quad için \quad F_L = 0{,}7F_y \tag{11}$$

$$L_r = 1{,}95 i_t \frac{E}{F_L} \sqrt{\frac{J}{W_{exc}h_0} + \sqrt{\left(\frac{J}{W_{exc}h_0}\right)^2 + 6{,}76\left(\frac{F_L}{E}\right)^2}} \tag{12}$$

$$\lambda = \frac{h_c}{t_w} \leq \lambda_{pw} \quad için \quad R_{pc} = \frac{M_p}{M_{yc}} \tag{13}$$

$$M_n = C_b\left[R_{pc}M_{yc} - (R_{pc}M_{yc} - F_L W_{exc})\left(\frac{L_b - L_p}{L_r - L_p}\right)\right] \leq R_{pc}M_{yc} \tag{14}$$

(iv) Built up II Section

The calculations for the Built up II section were performed using Equations (4, 7, 9, 10, 15–19):

$$L_r = \pi i_t \sqrt{\frac{E}{0{,}7F_y}} \tag{15}$$

$$F_{cr} = C_b\left[F_y - (0{,}3F_y)\left(\frac{L_b - L_p}{L_r - L_p}\right)\right] \leq F_y \tag{16}$$

$$a_w = \frac{h_c t_w}{b_{fc} t_{fc}} \leq 10 \tag{17}$$

$$R_{pg} = 1 - \frac{a_w}{1200 + 300a_w}\left(\frac{h_c}{t_w} - 5{,}7\sqrt{\frac{E}{F_y}}\right) \leq 1{,}0 \tag{18}$$

$$M_n = R_{pg}F_{cr}W_{exc} \tag{19}$$

(v) HE450A Section

The calculations for the HE450A section were performed using Equations (20):

$$M_n = M_p = F_y W_{py} \leq 1{,}6F_y W_{ey} \tag{20}$$

(vi) Box and Pipe Sections

The calculations for the Box and the Pipe sections were performed using Equations (21):

$$M_n = M_p = F_y W_p \tag{21}$$

In the equations, its denotes the effective radius of gyration, I_y is the moment of inertia about the y-axis, C_w is the warping constant, W_{ex} is the elastic section modulus about the x-axis, L_p represents the limiting laterally unbraced length for the yielding limit state, i_y is the radius of gyration about the y-axis, E is the modulus of elasticity (210000 MPa), F_y is the characteristic yield strength of the structural steel, L_r denotes the limiting laterally unbraced length for inelastic lateral-torsional buckling, J is the torsional constant, c = 1.0 for doubly symmetric I-sections, h_0 is the distance between the centroids of the flanges, C_b is the moment gradient factor, M_{max} is the maximum moment, M_A, M_B, and M_C are the moments along the beam span, F_{cr} is the critical buckling stress, L_b is the unbraced length of the member between points of lateral support, M_n is the nominal flexural strength, M_p is the plastic flexural moment, λ_f is the flange slenderness, λ_{pf} is the limiting slenderness for compact flanges, λ_{rf} is the limiting slenderness for noncompact flanges, it is the effective radius of gyration of the compression flange for lateral-torsional buckling limit state, b_{fc} is the width of the compression flange, h_c is twice the distance between the centroid and the end of curvature on the web near the compression flange, t_w is the web thickness, t_{fc} is the thickness of the compression flange, W_{ext} is the elastic section modulus about the x-axis for the tension zone, W_{exc} is the elastic section modulus about the x-axis for the compression zone, F_L is the reduced yield stress of the compression flange under bending, λ is the slenderness ratio, λ_{pw} is the limiting slenderness for compact webs, R_{pc} is the web plasticity coefficient, M_{yc} is the yield moment corresponding to yielding in the outer compression fiber, π is pi, a_w is the web-to-flange ratio parameter, R_{pg} is the web–flange interaction coefficient, W_{py} is the plastic section modulus about the minor principal axis, W_{ey} is the elastic section modulus about the minor principal axis, and W_p denotes the plastic section modulus.

2.6. Modelling

Seven steel beam elements, each 8 m in length and made of S235 steel grade, were modeled in SAP2000 with both ends fixed. The self-weight of the beam constitutes the G load, while a P load was applied at the midspan and an additional P_b load was applied at the outer edge of the top flange aligned with the midspan. The total mass of the model consists of the G, P, and P_b loads.

The locations where the P and P_b loads were applied are shown in Figure 1. The stress–strain curve of S235 steel is shown in Figure 2.

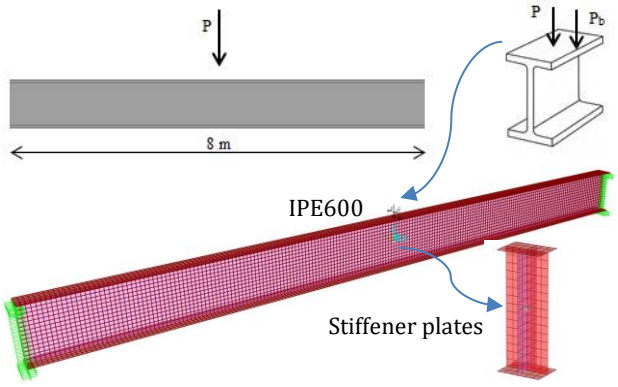

Figure 1. Beam model used in the analysis (L_b = 8 m, with P and P_b loads applied)

The vertical load (P) was applied at midspan through a transverse stiffener plate located between the flanges. To ensure realistic load transfer and avoid local stress concentration, a transverse stiffener plate

was modeled at the midspan between the flanges. The vertical load (P) was applied to this stiffener plate, allowing the load to be transferred uniformly to the web and flanges. The torsional load (P_b) was applied as a concentrated eccentric load at the outer edge of the top flange at midspan. This eccentric application introduced torsional effects about the longitudinal axis of the beam. The stiffener plate improved numerical stability and prevented artificial stress singularities that may occur due to single-node loading.

The transverse stiffener plate was modeled using four-node thin shell elements, consistent with the modeling approach adopted for the beam. The stiffener thickness was defined equal to the flange thickness for each corresponding cross-section model. The stiffener was connected to the web and flanges through common nodal connectivity to ensure compatible deformation and force transfer. In this respect, the stiffener was modeled following the same shell element formulation and discretization strategy as the beam elements. The vertical load (P) was applied as a static concentrated force to the stiffener nodes at midspan, allowing uniform load distribution to the web and flanges. The torsional load (P_b) was applied as a concentrated eccentric force at the outer edge of the top flange at midspan, generating torsional effects about the longitudinal axis of the beam.

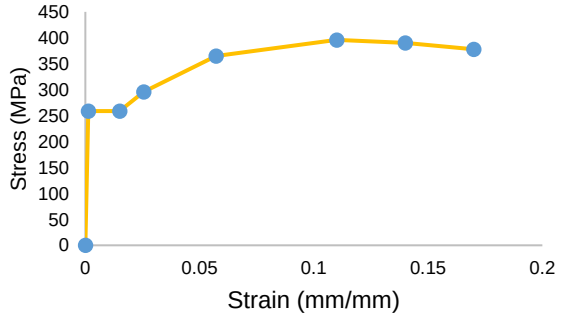

Figure 2. Stress–strain relationship of steel

The beam cross-sections were selected in accordance with the section classification requirements defined in Subsections 9.2–9.8 of Section 9 of reference [11]. Accordingly, IPE600 is a doubly symmetric I-shaped member classified as a compact section under bending about the major axis, as specified in Subsection 9.2. HE300AA is a doubly symmetric I-shaped member classified, according to Subsection 9.3, as having a compact web and a noncompact flange under bending about the major axis. Built up I is a singly symmetric I-shaped member, classified under Subsection 9.4, with a compact web under bending about the major axis.

Built up II is a doubly symmetric I-shaped member with a slender web, as defined in Subsection 9.5, under bending about the major axis. HE450A is an I-shaped member subjected to bending about the minor axis, as specified in Subsection 9.6. The box section is a doubly symmetric member classified, according to Subsection 9.7, as having compact web elements. The pipe section satisfies the compact section requirements in terms of the diameter-to-thickness ratio, as defined in Subsection 9.8. The cross-section types used in the study are presented in Table 1, and their geometric dimensions (in millimeters) are given in Table 2.

Table 1. Beam cross-sections

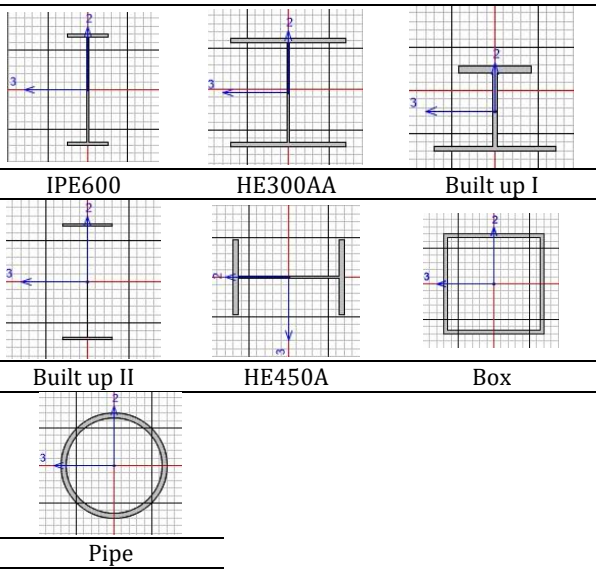

Table 2. Beam cross-section dimensions (mm)

Cross-section	IPE600	HE300AA	Built up I	Built up II
h	600	283	350	1650
b_f	220	300	300	700
t_f	19	10,5	30	25
t_w	12	7,5	15	10
b_{f2}	220	300	500	700
t_{f2}	19	10,5	20	25
f_r	0	0	0	0

Cross-section	HE450A	Box	Pipe
h	440	200	219,1
b_f	300	200	--
t_f	21	8	--
t_w	11,5	8	10
b_{f2}	300	200	--
t_{f2}	21	8	--
f_r	0	--	--

In Table 2, h denotes the total outer depth, b_f the width of the top flange, t_f the thickness of the top flange, t_w the web thickness, b_{f2} the width of the bottom flange, t_{f2} the thickness of the bottom flange, and f_r the fillet radius.

In the modeling process, shell elements were used, and each beam was modeled using shell elements with dimensions of 40 mm × 40 mm.

The number of shell elements used in the models is 5400 for IPE600, 4600 for HE300AA, 6000 for Built

up I, 15400 for Built up II, 5400 for HE450A, 4000 for the box section, and 4800 for the pipe. For the shell elements, the thickness values corresponding to the flanges and the web were defined; the number of layers in the shell elements was taken as one, and the material behavior was modeled as nonlinear.

In the finite element modeling, all beams were discretized using four-node shell elements available in SAP2000. Thin-shell formulation was adopted, assuming that transverse shear deformation effects were negligible relative to bending behavior. The web and flange plates were modeled explicitly as separate shell surfaces and connected through shared nodes along their intersection lines, ensuring full compatibility between elements. No rigid links were used between web and flanges.

A structured mesh with an approximate element size of 40 mm × 40 mm was employed along the beam length and cross-section. A preliminary mesh sensitivity study indicated that further mesh refinement produced changes of less than 2% in the maximum load values; therefore, this mesh density was considered sufficient for accuracy and computational efficiency. To ensure numerical reliability, a mesh convergence study was performed on representative sections (IPE600 and Built up II). In addition to the adopted 40 mm × 40 mm mesh size, refined meshes of 30 mm × 30 mm and 20 mm × 20 mm were analyzed. The comparison demonstrated that the variation in maximum load capacity remained below 2%, the difference in displacement values was less than 2.5%, and the change in buckling factors did not exceed 1.8%. Although finer meshes increased computational time significantly, no meaningful improvement in accuracy was observed. Therefore, the 40 mm × 40 mm mesh size was considered sufficient to ensure mesh-independent and computationally efficient results.

Both ends of the beams were modeled as fully fixed supports by restraining all translational and rotational degrees of freedom. Regarding boundary conditions, supports for the shell elements were defined at the nodal level by restraining the corresponding degrees of freedom. The fixed (fully clamped) support condition was modeled by constraining all translational degrees of freedom (Ux, Uy, Uz) and all rotational degrees of freedom (Rx, Ry, Rz) at the supported nodes. This definition ensures that both in-plane and out-of-plane displacements, as well as rotations of the shell elements, are fully restrained, thereby representing a classical fixed-end boundary condition.

The vertical load (P) was applied as a nodal load distributed along the top flange width at midspan, while the torsional load (P_b) was applied eccentrically at the outer edge nodes of the compression flange to induce torsion. Warping deformation was not explicitly constrained; thus, torsional behavior developed naturally according to the shell stiffness formulation. These modeling assumptions allow realistic simulation of bending, torsional, and lateral–torsional buckling behavior while maintaining computational consistency.

In the numerical implementation, geometric nonlinearity (P–Delta effects) was activated in all second-order analyses. Material nonlinearity was defined using a bilinear stress–strain model for S235 steel, incorporating strain hardening behavior. An elastic modulus of 210,000 MPa was adopted up to the yield stress of 235 MPa, followed by a positive post-yield tangent modulus to represent strain hardening [3]. This bilinear elastic–plastic model enables a more realistic representation of the post-yield structural response under increasing load levels.

The shell elements were assigned nonlinear material properties, and displacement-controlled loading was applied at the midspan to capture post-yield behavior. The convergence criteria were based on force and displacement tolerances automatically defined in SAP2000. For buckling analyses, eigenvalue buckling was performed using the stiffness matrix obtained from the nonlinear static solution under the relevant load combination. Only the first mode was evaluated in determining the critical buckling factor. No initial geometric imperfections were introduced into the models; therefore, the results represent idealized structural behavior under perfect geometry assumptions. The omission of initial geometric imperfections was intentional, as the primary objective of this study was to establish a direct comparison between code-based theoretical predictions and nonlinear finite element results under idealized geometric conditions. Introducing imperfections would require assumptions regarding amplitude and shape, which could introduce additional parameters affecting the comparison. It is acknowledged that geometric imperfections may reduce the load-carrying capacity, particularly in slender sections such as Built up II, and their inclusion would likely lead to lower ultimate capacities. However, the present study focuses on evaluating the inherent differences between analytical formulations and nonlinear numerical modeling without additional imperfection sensitivity parameters. The influence of geometric imperfections may be considered in future investigations.

The beam length (L_b = 8 m) was not selected arbitrarily. According to the provisions of the Regulation on Design, Calculation, and Construction Principles of Steel Structures [11] (Clause 9.5), the flexural strength of steel beams under lateral–torsional buckling depends on the relationship between the unbraced length (L_b) and the limiting

lengths L_p and L_r. When $L_b \leq L_p$, the beam reaches its full plastic moment capacity (M_p). When $L_p < L_b < L_r$, inelastic lateral–torsional buckling governs. When $L_b \geq L_r$, elastic lateral–torsional buckling becomes dominant.

Preliminary calculations performed for the investigated cross-sections indicated that an 8 m unbraced length places several sections within the inelastic and elastic lateral–torsional buckling regions ($L_b \approx L_r$ for slender-web sections), while compact sections remain near the plastic transition zone. Therefore, this span length enables the simultaneous observation of plastic capacity limits and stability-controlled behavior within the same analytical framework.

In this respect, the selected 8 m length is directly related to the critical buckling length parameters defined in the design code and allows meaningful evaluation of the interaction between second-order effects and lateral–torsional buckling behavior.

3. Analyses

3.1. Second-order plastic analysis

For the second-order plastic analysis, the first loading case was solved for the G+P combination, with the geometric nonlinearity parameter (P-Delta) activated and the analysis type defined as nonlinear.

In the second loading case, the initial conditions were taken as G+P, the modal load case was defined based on modal analysis (12 modes), the geometric nonlinearity parameter (P-Delta) was again activated, the analysis type was set to nonlinear, and the load application method was specified as displacement control. Thus, both geometric and material nonlinear behaviors were incorporated into the model.

A vertical load P applied at the midspan of the beam was incrementally increased, and the displacement values at the bottom midpoint of the beam were monitored during this process. Using the obtained P–displacement (Δ) data pairs, the performance curve of the beam was constructed. The load value corresponding to the end of the linear portion of the performance curve was identified as the yield load (P_y), and its corresponding displacement was defined as the yield displacement (Δ_y). Similarly, the final load value at the end of the curve was taken as the maximum load (P_{max}), and its corresponding displacement was defined as the maximum displacement (Δ_{max}).

Since the performance curves of the beams exhibit different magnitudes, some curves have significantly higher values while others are relatively low. As a result, presenting all curves on a single graph would make it difficult to interpret the results clearly. Therefore, the performance curve of each beam was plotted individually. The performance curves corresponding to the beam types are presented in Figure 3–9.

In response to the reviewer's comment, the stress contour figures were revised to improve interpretability. However, instead of presenting stress–strain field readings, which may not directly reflect global structural behavior, load–displacement curves were introduced for each section. These curves clearly demonstrate stiffness degradation, nonlinear response, and ultimate capacity, providing a clearer and more direct insight into the overall structural behavior compared to isolated stress contour plots.

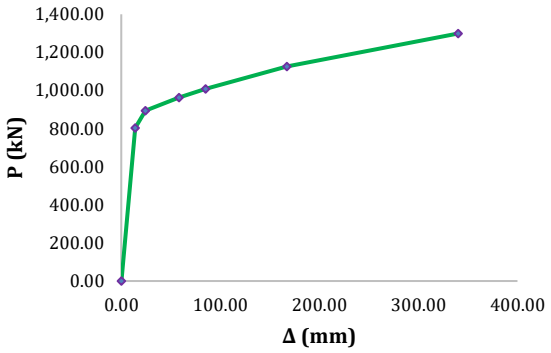

Figure 3. Performance curve of the IPE600 beam

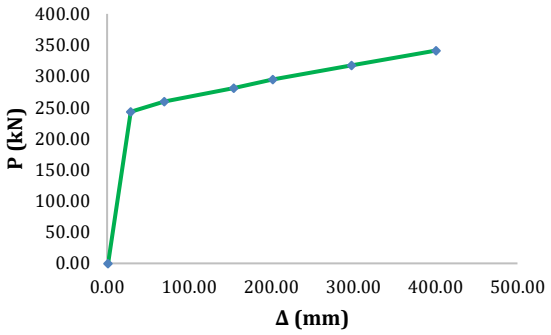

Figure 4. Performance curve of the HE300AA beam

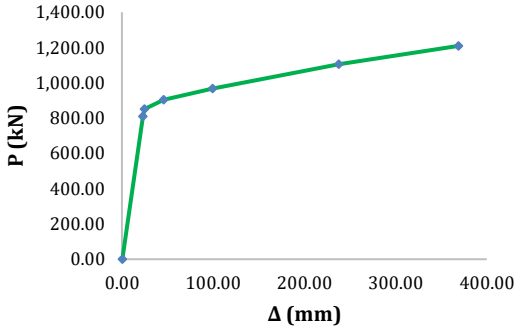

Figure 5. Performance curve of the Built up I beam

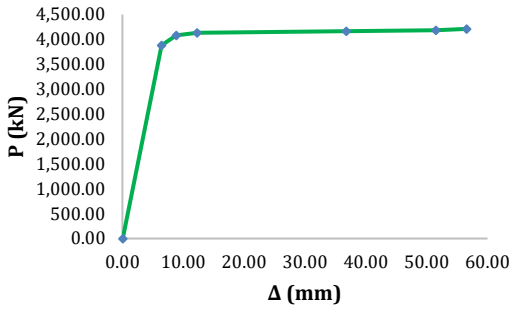

Figure 6. Performance curve of the Built up II beam

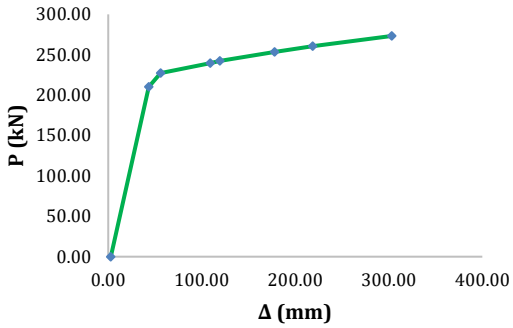

Figure 7. Performance curve of the HE450A beam

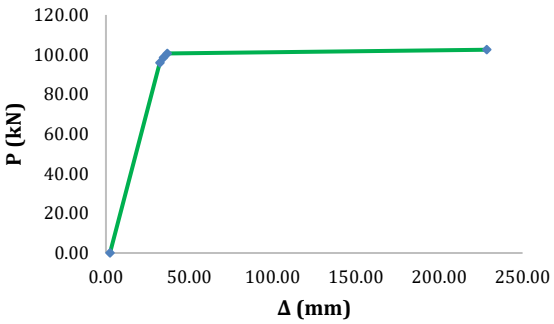

Figure 8. Performance curve of the Box beam

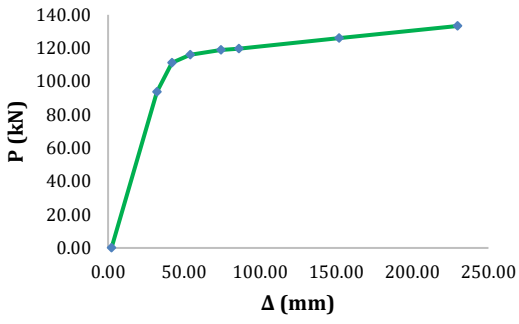

Figure 9. Performance curve of the Pipe beam

The analyses were performed using displacement-controlled nonlinear static analysis. Therefore, a clear descending branch is not always observed in the load–displacement curves. The maximum load-carrying capacity was defined as the peak load obtained from the load–displacement curve. The failure criterion corresponds to the ultimate displacement at which significant stiffness degradation and stability loss occurred.

Second-order plastic analyses represent an advanced method that provides a more realistic understanding of beam behavior under loading. In this approach, not only elastic limits but also the effects of large displacements and the formation of plastic hinges along the cross-sections are taken into account. The diagrams obtained from these analyses visually illustrate the deformed shapes of the beams and the stress distributions along their cross-sections, thereby allowing a detailed examination of the structural behavior.

These results provide significant insights, particularly for identifying stability limits and collapse mechanisms, and contribute to the accurate prediction of load-carrying capacity and the safe design of engineering structures. The diagrams related to the deformation and stress distribution are presented below.

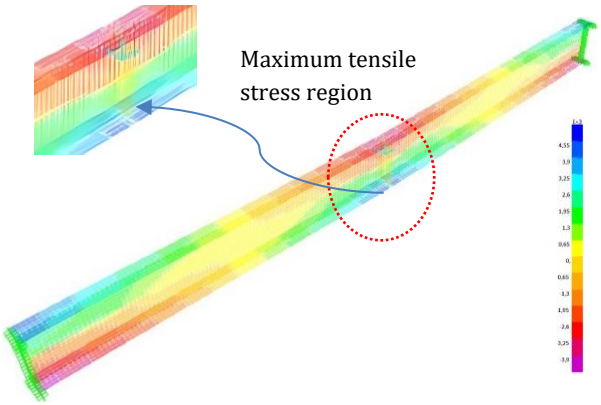

Figure 10. Stress diagrams of IPE600 beam

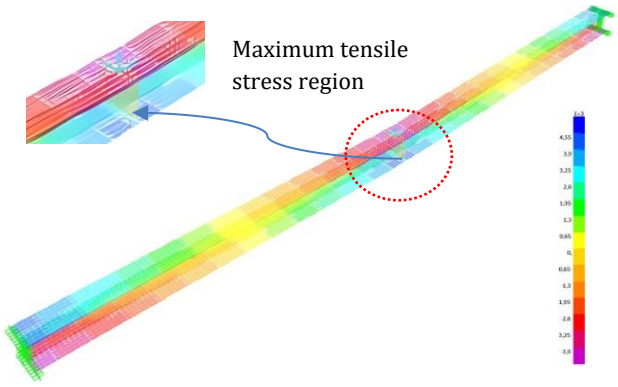

Figure 11. Stress diagrams of HE300AA beam

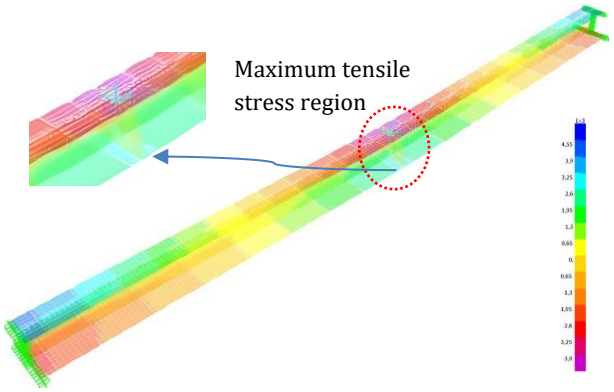

Figure 12. Stress diagrams of Built up I beam

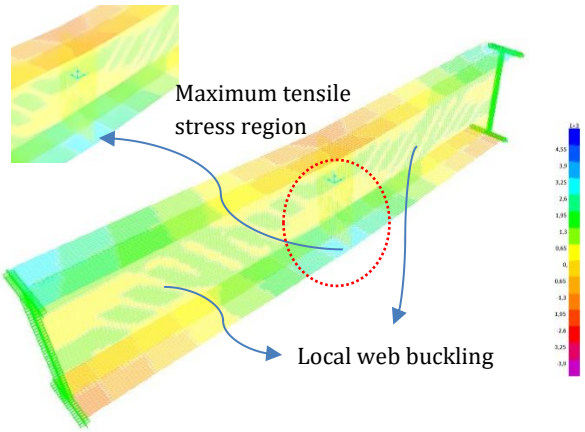

Figure 13. Stress diagrams of Built up II beam

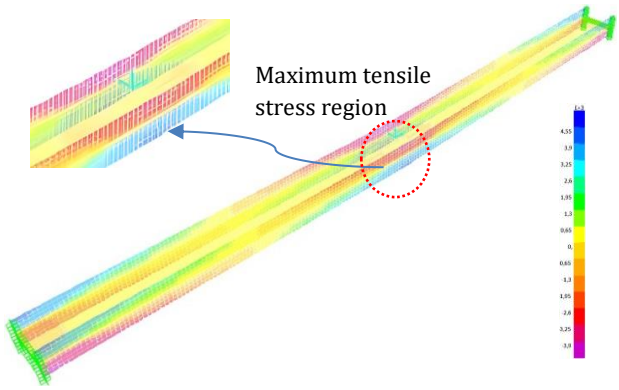

Figure 14. Stress diagrams of HE450A beam

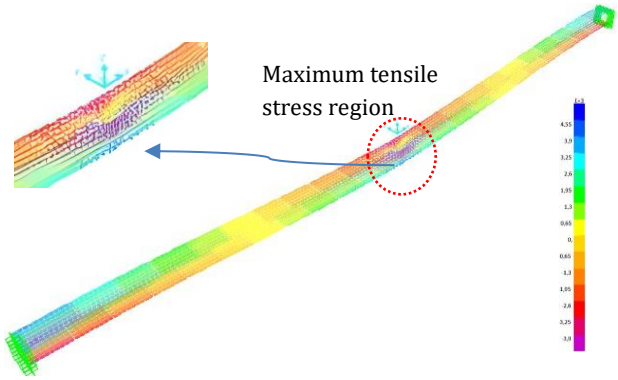

Figure 15. Stress diagrams of Box beam

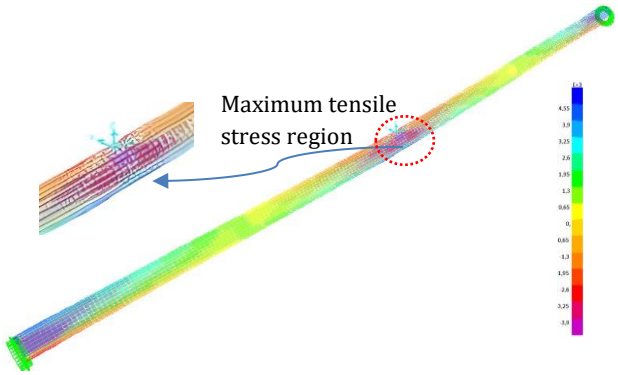

Figure 16. Stress diagrams of Pipe beam

3.2. Buckling analysis

Buckling analysis was conducted for flexural, torsional, and lateral-torsional buckling modes. In the flexural buckling analysis, the G and P loads were considered; in the torsional buckling analysis, the G and P_b loads were considered; and in the lateral-torsional buckling analysis, the G, P, and P_b loads were taken into account. Here, the P load induces bending in the beam, while the P_b load causes torsion. The first step of the buckling analysis consists of a static analysis, in which the modal load case was defined based on modal analysis (12 modes), and the geometric nonlinearity parameter (P-Delta) was activated. The second step involves the buckling analysis itself, which was performed as a linear buckling analysis in SAP2000. It should be noted that no buckling factor was obtained for the pipe beam.

It should be noted that SAP2000 was unable to compute the buckling factor for the pipe section. This limitation is not due to a software error but results from the closed and highly symmetric nature of the pipe cross-section. Pipe sections possess high torsional rigidity, and the standard linear elastic eigenvalue (buckling) analysis in SAP2000 is primarily formulated for open sections such as I or box profiles, where lateral supports and degrees of freedom align with the underlying assumptions. For pipe sections, the first torsional or lateral-torsional mode occurs at a very high critical load, which the software does not resolve within the linear eigenvalue framework. Therefore, the stability behavior of the pipe section was instead evaluated through load–displacement curves obtained from the second-order plastic analysis, providing a reliable and sufficient assessment of the beam's load-carrying capacity and overall response.

In the flexural buckling analysis, the static analysis was performed under the G+P load combination, and in the second step, the 'stiffness to use' option was set to the G+P solution, with the analysis carried out for one mode. In the torsional buckling analysis, the static analysis was performed under the G+P_b load combination, and in the second step, the 'stiffness to

use' option was set to the G+P_b solution, again for one mode.

In the lateral-torsional buckling analysis, the static analysis was performed under the G+P+P_b load combination, and in the second step, the 'stiffness to use' option was set to the G+P+P_b solution, with the analysis performed for one mode. Buckling analysis is one of the fundamental methods used to determine the stability loss behavior of beams under critical loading conditions. Within this analysis, not only the elastic deformations of the structure but also the points at which the equilibrium configuration becomes unstable are considered. The obtained results reveal the buckling modes of the beams and the corresponding critical load values, thereby shedding light on one of the key factors that limit the load-carrying capacity of structural members. The resulting mode shapes visually demonstrate the buckling forms through which the structure loses stability and contribute to the accurate determination of safety factors during the design process. In this context, the mode shapes related to the lateral-torsional buckling behavior of the beams are presented below.

Local buckling modes observed near the support regions differ depending on the cross-sectional characteristics of each beam model. For the HE300AA section, the flange is classified as non-compact. Under high compressive stresses developing near the supports, this non-compact flange becomes susceptible to local buckling, leading to localized instability before full plastic redistribution can occur. In the case of the HE450A section, the relatively lower weak-axis stiffness contributes to increased sensitivity to combined compression and torsional effects near the supports. The interaction of bending and torsional stresses in this region promotes local stability loss. The Built-up II section consists of slender plate elements with relatively high width-to-thickness (b/t) ratios. Due to its slender nature, local plate buckling becomes the governing mechanism under compressive stresses concentrated at the support zones. Although box sections exhibit high torsional rigidity and strong resistance against global lateral–torsional buckling due to their closed geometry, thin-walled behavior may lead to local panel buckling under the combined action of compressive and shear stresses near the supports. These observations indicate that the local buckling behavior is primarily governed by element slenderness, plate stability characteristics, and stress concentration effects in the support regions.

To further address the reviewer's comment, the first buckling mode shapes were presented to illustrate the governing instability mechanisms. This approach offers a more comprehensive understanding of both global structural behavior and instability characteristics, linking local stress patterns to global stability phenomena more effectively than isolated stress contour plots.

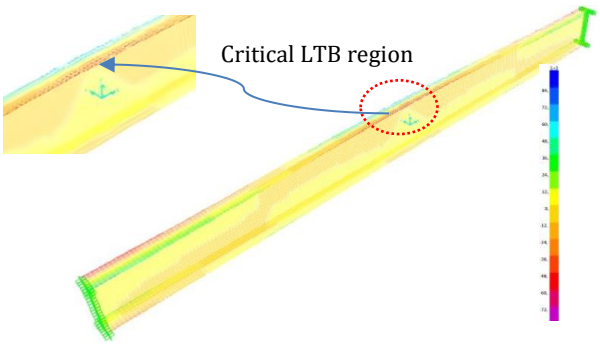

Figure 17. Stress diagrams of IPE600 beam in lateral-torsional buckling case

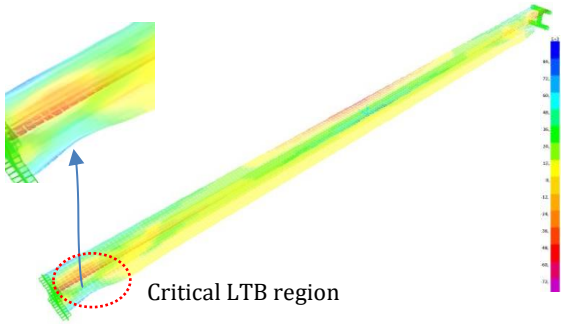

Figure 18. Stress diagrams of HE300AA beam in lateral-torsional buckling case

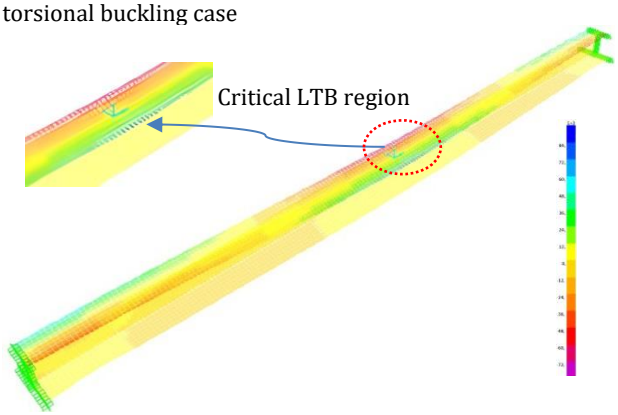

Figure 19. Stress diagrams of Built up I beam in lateral-torsional buckling case

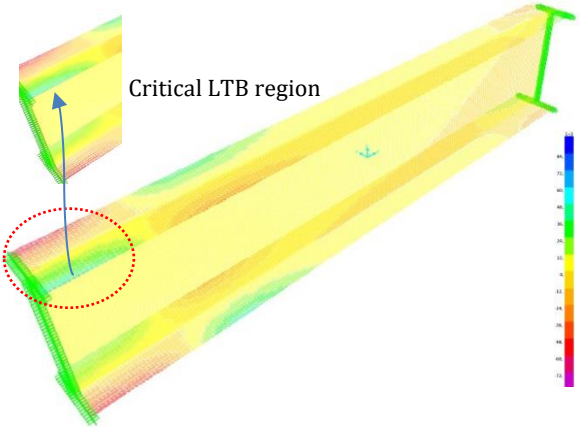

Figure 20. Stress diagrams of Built up II beam in lateral-torsional buckling case

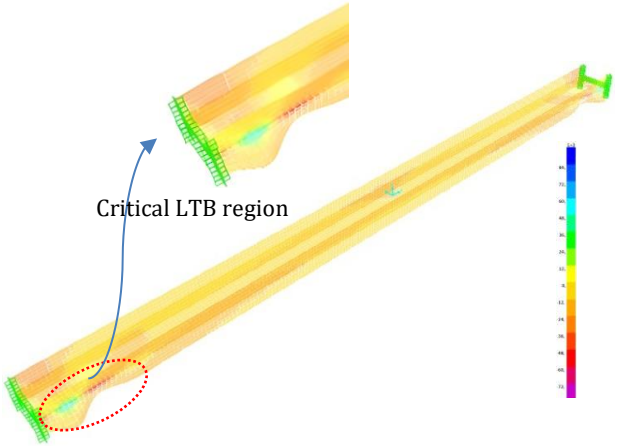

Figure 21. Stress diagrams of HE450A beam in lateral-torsional buckling case

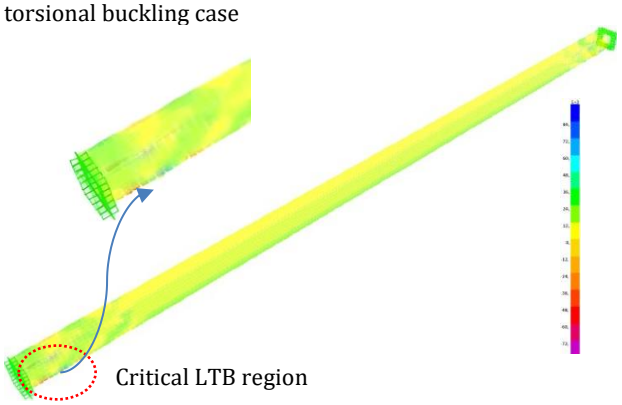

Figure 22. Stress diagrams of Box beam in lateral-torsional buckling case

4. Findings

4.1. Results of theoretical calculations

The calculation equations used for each beam are presented in Section 2.5, and the obtained values of characteristic bending moment capacity (M_n) and plastic bending moment (M_p) are summarized in Table 3. These theoretical values were compared with the numerical analysis results obtained through the SAP2000 software. In this way, the effects of geometric and material properties of different cross-section types on moment capacity were evaluated both analytically and numerically.

Table 3. Moment values (kNm)

Moment	IPE600	HE300AA	Built up I	Built up II
M_n	1.107,81	236,16	1.710,26	7.554,35
M_p	825,32	250,27	800,37	8.186,81
Moment	HE450A	Box	Pipe	
M_n	237,26	94,00	96,35	
M_p	227,01	94,00	96,35	

The smaller of the M_n and M_p values represents the maximum moment capacity adopted in the design.

In order to properly interpret the theoretical bending resistance results, the slenderness characteristics and lateral–torsional buckling regions of all beam models were evaluated in accordance with Section 9.2.2 of the Regulation on Design, Calculation, and Construction Principles of Steel Structures [11]. The flange and web slenderness ratios were calculated for each cross-section to determine section classification and local stability behavior. All models were analyzed using S235 steel with a constant unbraced length of Lb = 8 m. The unbraced length was compared with the limiting buckling lengths defined in the Regulation to determine the position of each section on the characteristic bending moment resistance curve.

Based on this assessment, IPE600, HEA450, box, pipe, and Built-up I sections fall within the elastic lateral–torsional buckling region, whereas HE300AA and Built-up II sections fall within the inelastic lateral–torsional buckling region. This classification establishes the theoretical stability framework used to interpret the calculated bending resistances and to explain the differences observed among the cross-sections.

4.2. Results of second-order plastic analysis

Within the scope of the analyses, the yield loads, maximum displacement values, and the load levels corresponding to the ultimate load-carrying capacity were determined. The obtained results reveal the transition of the beams from the elastic range to plastic behavior, as well as the load–displacement relationship up to the failure capacity. The results for yield load, yield displacement, maximum load, and maximum displacement are presented in Table 4.

Table 4. Load (kN) – displacement (mm) values

Beam	IPE600	HE300AA	Built up I	Built up II
P_y	803,75	242,89	808,75	3.885,58
P_{max}	1.299,34	341,21	1.209,20	4.347,50
Δ_y	13,94	28,76	22,95	6,45
Δ_{max}	340,29	401,00	369,00	71,69
Beam	HE450A	Box	Pipe	
P_y	210,23	95,84	93,78	
P_{max}	273,23	102,46	133,29	
Δ_y	43,27	32,38	32,02	
Δ_{max}	303,00	228,37	229,61	

By applying the G load and the P_y value given in Table 4 to the beam element, the corresponding moment values were calculated, and thus the yield moments (M_y) associated with the P_y load were obtained.

The moment values (M_y) for the midspan and support regions are presented in Table 5, where it was observed that the M_y value at midspan is lower than that at the support. In this context, the M_y value obtained at midspan is considered as the moment value adopted in the design.

Table 5. M_y values (kNm)

Moment	IPE600	HE300AA	Built up I	Built up II
M_y (midspan)	806,95	244,71	813,57	3.896,05
M_y (support)	810,15	246,54	818,40	3.906,52
Moment	HE450A	Box	Pipe	
M_y (midspan)	213,88	96,73	95,13	
M_y (support)	217,54	97,99	96,48	

4.3. Analytical and numerical comparison

In this section, "analytical results" refer to the bending resistance values calculated according to the Regulation on Design, Calculation, and Construction Principles of Steel Structures, whereas "numerical results" correspond to the ultimate bending capacities obtained from displacement-controlled nonlinear finite element analyses.

The comparison is presented by listing both values explicitly and calculating the percentage difference between analytical and numerical results for each cross-section.

The smaller value between M_n and M_p given in Table 3 was compared with the midspan M_y value presented in Table 5, as both represent the values adopted in the design.

Table 6. Compared moment values (kNm)

Beam	IPE600	HE300AA	Built up I	Built up II
M_y (midspan)	806,95	244,71	813,57	3.896,05
M_n-M_p (the smaller one)	825,32	236,16	800,37	7.554,35
Percentage difference	2,27	3,62	1,64	93,89
Beam	HE450A	Box	Pipe	
M_y (midspan)	213,88	96,73	95,13	
M_n-M_p (the smaller one)	227,01	94,00	96,35	
Percentage difference	6,13	2,90	1,28	

Table 6 presents the yield moments at midspan (M_y), the theoretical characteristic and plastic moment values (M_n–M_p), and the differences between these values. For most beams, the difference between M_y and M_n–M_p is around 1–6%, indicating a high agreement between the theoretical calculations and the SAP2000 analysis results.

In particular, for the IPE600, HE300AA, Built up I, Box, and Pipe beams, the differences are quite small, and the midspan moments can be reliably used as the governing design moments.

In contrast, the difference for the Built up II beam reaches a significant 93.89%, highlighting that second-order effects and buckling factors play a critical role in the calculations. However, this large discrepancy cannot be attributed solely to second-order (P–Delta) effects. The Built up II section is characterized by a slender web classified under Subsection 9.5, making it highly susceptible to local plate buckling before the full plastic moment capacity can be developed. The nonlinear finite element results indicate a strong interaction between local web buckling, global lateral–torsional buckling, and geometric nonlinearity. In contrast, the code-based formulation idealizes the transition between inelastic and elastic lateral–torsional buckling regions and does not explicitly capture the coupled influence of local instability and global second-order behavior. Therefore, the observed 93.89% difference primarily arises from the combined interaction of local slenderness effects and global stability phenomena, rather than from second-order effects alone. The moment values presented in Table 6 are also illustrated in Figure 23 as a comparative bar chart, based on the SAP2000 analysis and the calculations from [11].

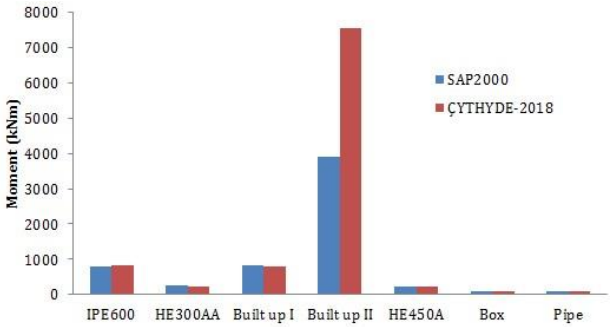

Figure 23. Midspan M_y and M_n - M_p values for different beam sections (kNm)

4.4. Results of buckling analysis

Within the scope of the buckling analysis, the critical load factors (buckling factors), which describe the stability behavior of the beams, were obtained. These factors indicate the load levels at which the structure reaches equilibrium instability within the elastic range and provide important information for assessing the risk of beam failure. The buckling factors obtained from the analyses are presented in Table 7, with the corresponding values reflecting the stability capacity of the beams under different buckling modes. The buckling factors shown in Table 7 are also illustrated in Figure 24 as a comparative bar chart.

Table 7. Buckling factors

Beam	Flexural buckling	Torsional buckling	Lateral-torsional buckling
IPE600	245,73	245,66	185,97
HE300AA	197,70	168,17	141,73
Built up I	2.174,10	494,20	429,25
Built up II	101,11	101,10	96,81
HE450A	493,24	449,90	400,88
Box	249,36	249,33	193,44
Pipe	---	---	---

For the tube-section beam, although 200 modes were considered, SAP2000 did not calculate a buckling factor. In the IPE600, Built up II, and Box beams, the buckling factors for the flexural and torsional buckling modes were very close to each other (< 1% difference). For the Built up I beam, the difference between the torsional and lateral-torsional buckling modes was 15.13%, whereas the difference compared to the flexural buckling mode reached 339.92%.

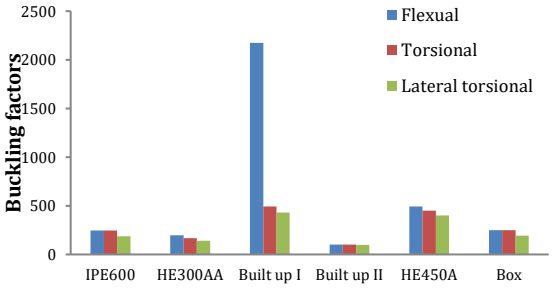

Figure 24. Buckling factors

4.5. Discussion on the applicability and limitations of the regulation

The comparative results obtained from theoretical calculations and nonlinear numerical analyses indicate certain discrepancies in the bending resistance predictions for some cross-sections. While the Regulation on Design, Calculation, and Construction Principles of Steel Structures [11] provides a consistent stability framework, differences observed particularly in inelastic lateral–torsional buckling regions suggest that the current formulation may not fully capture the behavior of certain non-compact and built-up sections.

For example, sections classified within the inelastic buckling region exhibited capacity trends that differ from the simplified transition assumptions defined in the Regulation. In addition, local buckling effects observed in slender and partially compact sections indicate that the interaction between local plate instability and global lateral–torsional buckling may require more refined treatment.

These findings suggest that further calibration studies incorporating advanced nonlinear analyses and experimental validation could contribute to improving the accuracy of bending resistance predictions. Therefore, limited revisions or refinements in the treatment of stability transition regions and slender built-up members may enhance the reliability of the Regulation.

The findings obtained in this study are generally consistent with previous research on second-order effects and buckling behavior of slender steel members. Similar to the literature, the results confirm that geometric nonlinearity significantly reduces the load-carrying capacity of slender sections and that cross-sectional geometry plays a decisive role in overall stability performance. The pronounced influence of second-order effects observed in the Built up II section aligns with earlier numerical and theoretical studies emphasizing the sensitivity of slender web configurations to stability-related reductions in strength.

However, the present study differs from existing literature by directly comparing the theoretical moment capacities prescribed in the Regulation on Design, Calculation, and Construction Principles of Steel Structures [11] Subsection 9.5 with the results of second-order plastic analyses for different cross-section types. The substantial deviation (93.89%) identified for the Built up II section indicates that the code-based formulation may not adequately represent the actual structural behavior of certain slender configurations. In this respect, the study not only confirms established stability trends reported in the literature but also contributes by critically evaluating the applicability and limitations of the current design provisions.

5. Conclusions

In this study, seven steel beams with a length of 8 m and made of S235 steel were examined, each fixed at both ends. The beam cross-sections were selected to satisfy the section requirements defined in Subsections 9.2–9.8 of Section 9 of the Regulation on the Design, Calculation, and Construction of Steel Structures [11].

Considering the relevant provisions of the regulation:

- In the IPE600 section, both the web and flanges are compact.
- In the HE300AA section, the web is compact, while the flanges are non-compact.
- In the Built up I section, both the web and flanges are compact.
- In the Built up II section, the web is slender, and the flanges are non-compact.
- In the HE450A section, both the web and flanges are compact.
- In the Box and Pipe sections, both elements are classified as compact.

In this study, the load-carrying behavior of the beams was evaluated comparatively using different analysis methods. The theoretical calculation results were compared with the second-order plastic analysis results; additionally, within the scope of the buckling analysis, beams with different cross-section classes were compared among themselves.

Examination of the theoretical calculations and second-order plastic analysis results shows a high agreement in terms of the maximum moment capacity adopted in the design for the IPE600, HE300AA, Built up I, HE450A, Box, and Pipe beams. In contrast, a significant discrepancy was observed for the Built up II beam, which was found to result from the determining effect of second-order effects and buckling factors on the calculations. Furthermore, this finding indicates the need to update the equations presented in Subsection 9.5 of the regulation.

For the pipe section beam, the buckling factor could not be calculated, while for all other beam types, the smallest buckling factor was observed in the lateral-torsional buckling mode. Accordingly, the critical buckling mode was determined to be the lateral-torsional buckling mode.

As a result of the buckling analysis performed on the Built up I beam, the buckling factors for the flexural, torsional, and lateral-torsional buckling modes were obtained as 2,174.10, 494.20, and 429.26, respectively.

The high buckling factor in the flexural mode indicates that the cross-section is very stiff against uniaxial bending, and the tendency for buckling in this mode is low. In contrast, the significantly lower values observed for the torsional and lateral-torsional modes indicate that the torsional stiffness of the section is limited, making it more likely that stability loss occurs in these modes.

Since the lowest buckling factor was obtained in the lateral-torsional buckling mode (429.26), this mode was identified as the critical buckling mode. This finding demonstrates that the Built up I section exhibits sensitivity to combined lateral displacement and torsion effects.

For the Built up II beam, the buckling factors in the flexural and torsional modes are nearly identical, with the difference being negligible (~0.01%). In contrast, the lateral-torsional buckling factor is approximately 4.43% lower than these two values. These results indicate that the Built up II section generally exhibits a balanced stability level across the modes, but the initial stability loss is most likely to occur in the lateral-torsional buckling mode.

Examination of the theoretical calculations and second-order plastic analysis results shows that the beam transitions to a mechanism state without plastic deformation, highlighting that this section is more sensitive to buckling, and that buckling checks are critical in design.

Consequently, for the Built up II beam, second-order effects, local buckling, and lateral-torsional interactions should be considered in the design. If necessary, section stiffness should be increased, support spans reduced, or reinforcement elements should be provided to enhance lateral-torsional stiffness.

The theoretical calculations, second-order plastic analyses, and buckling analyses conducted on the steel beams examined in this study have provided comprehensive insights into their load-carrying and stability behavior. The beams with IPE600, HE300AA, Built up I, HE450A, Box, and Pipe sections exhibited high agreement between the theoretical and numerical analyses in terms of their maximum moment capacities.

In contrast, for the Built up II beam, the agreement was significantly reduced due to the determining effects of second-order phenomena and buckling factors, and the section demonstrated higher sensitivity to buckling. These findings clearly indicate that, in beam design, slender web sections should be avoided, and sections with compact webs and flanges should be preferred.

Declaration of Ethical Code

In this study, we undertake that all the rules required to be followed within the scope of the "Higher Education Institutions Scientific Research and Publication Ethics Directive" are complied with, and that none of the actions stated under the heading "Actions Against Scientific Research and Publication Ethics" are not carried out.

References

[1] Timoshenko, S. P., Gere, J. M. 1961. Theory of elastic stability (2nd ed.). McGraw-Hill.

[2] Trahair, N. S. 1993. Flexural-torsional buckling of structures. CRC Press.

[3] EN 1993-1-1. 2005. Eurocode 3: Design of steel structures – Part 1-1: General rules and rules for buildings. European Committee for Standardization.

[4] Sun, H., Wang, Y., Zhou, L. 2023. Experimental study on lateral restraints of continuous steel beams. Engineering Structures, 286, 116002.

[5] Zhang, Y., Li, H., Xu, C. 2018. Experimental and numerical investigation on lateral-torsional

buckling of steel beams under impact loading. Engineering Structures, 167, 10–22.

[6] Mascolo, I., Camotim, D., Silvestre, N. 2018. Effects of imperfections and loading eccentricities on the distortional buckling resistance of C-section beams. Thin-Walled Structures, 127, 359–371.

[7] Andrade, A., Camotim, D. 2005. Numerical evaluation of the lateral–torsional buckling behaviour of steel I-beams. Computers & Structures, 83(7–8), 596–615.

[8] Kabir, M. Z., Seif, A. E. 2011. Lateral torsional buckling of steel I-beam retrofitted using FRP sheets: Analytical solution and optimization. In Ye, L., Feng, P., Yue, Q. (Eds.), Advances in FRP Composites in Civil Engineering, 1225–1228. Springer.

[9] Chen, W. F., Sohal, I. 1995. Plastic design and second-order analysis of structures. Springer.

[10] Galambos, T. V. 1998. Guide to stability design criteria for metal structures (5th ed.). John Wiley & Sons.

[11] Türkiye Cumhuriyeti Çevre ve Şehircilik Bakanlığı. 2018. Çelik Yapıların Tasarım, Hesap ve Yapımına Dair Esaslar (ÇYTHYDE-2018).

[12] Bradford, M. A. 1992. Inelastic buckling of steel structures. Journal of Constructional Steel Research, 22(1–3), 95–112.

[13] Fu, Z.-F., He, J. 2001. Modal analysis. Butterworth-Heinemann.

[14] Liew, J. Y. R. 1993. Second-order refined plastic-hinge analysis for frame structures. Journal of Structural Engineering, 119(11), 3217–3236.

[15] King, W. 1990. Simplified Second-Order Inelastic Analysis for Frame Design. Purdue University Dissertations.

[16] CSI. 2020. SAP2000 Integrated Software for Structural Analysis and Design – Analysis Reference Manual. Computers and Structures Inc., Berkeley, California.

[17] Cook, R. D., Malkus, D. S., Plesha, M. E., Witt, R. J. 2007. Concepts and Applications of Finite Element Analysis. 4th Edition, Wiley.

[18] Chajes, A. 1998. Principles of Structural Stability Theory. Prentice Hall.